Quantitative atomic force microscopy provides new insight into matrix vesicle mineralization

Quantitative Atomic Force Microscopy Provides New Insight into Matrix Vesicle Mineralization

Justin S. Plaut,[a,b] Agnieszka Strzelecka-Kiliszek,[c] Lukasz Bozycki,[c] Slawomir Pikula,[c] René Buchet,[d] Saida Mebarek,[d] Meriem Chadli,[d] Maytê Bolean,[e] Ana M. S. Simao,[e] Pietro Ciancaglini,[e] Andrea Magrini,[f,g] Nicola Rosato,[g,h] David Magne,[e] Agnès Girard-Egrot,[e] Colin Farquharson,[i] Sadik C. Esener,[a,b] José L. Millan,[j] Massimo Bottini[,g,h,j]*

[a] Cancer Early Detection Advanced Research Center, Knight Cancer Institute, Oregon Health & Science University, Portland, Oregon 97201, USA

[b] Department of Bioengineering, University of California San Diego, La Jolla, California 92093, USA

[c] Laboratory of Biochemistry of Lipids, Nencki Institute of Experimental Biology, Polish Academy of Sciences, 02-093 Warsaw, Poland

[d] Université de Lyon, Université Lyon 1, Institut de Chimie et Biochimie Moléculaires et Supramoléculaires, UMR CNRS 5246, 69 622 Villeurbanne Cedex, France

[e] Faculdade de Filosofia, Ciências e Letras de Ribeirão Preto – USP, Departamento de Química, 14040-901 Ribeirão Preto, Brasil

[f] Department of Biopathology and Imaging Diagnostics, University of Rome Tor Vergata, Rome, Italy

[g] Nanoscience & Nanotechnology & Innovative Instrumentation (NAST) Centre, University of Rome Tor Vergata, Rome, Italy

[h] Department of Experimental Medicine, University of Rome Tor Vergata, Rome, Italy

[i] Division of Developmental Biology, The Roslin Institute and Royal (Dick) School of Veterinary Studies, University of Edinburgh, Easter Bush, Roslin, Midlothian, Edinburgh EH25 9RG, UK

[j] Sanford Burnham Prebys Medical Discovery Institute, La Jolla, CA 92037, USA

Corresponding Author

*Department of Experimental Medicine, University of Rome Tor Vergata, Via Montpellier, 1, 00133 Rome, Italy. E-mail: massimo.bottini@uniroma2.it.

ABSTRACT

Matrix vesicles (MVs) are a class of extracellular vesicles that initiate mineralization in cartilage, bone, and other vertebrate tissues by accumulating calcium ions (Ca^{2+}) and inorganic phosphate (P_i) within their lumen and forming a nucleation core (NC). After further sequestration of Ca^{2+} and P_i, the NC transforms into crystalline complexes. Direct evidence of the existence of the NC and its maturation have been provided solely by analyses of dried samples. We isolated MVs from chicken embryo cartilage and used atomic force microscopy peak force quantitative nanomechanical property mapping (AFM-PFQNM) to measure the nanomechanical and morphological properties of individual MVs under both mineralizing ($+Ca^{2+}$) and non-mineralizing ($–Ca^{2+}$) fluid conditions. The elastic modulus of MVs significantly increased by 4-fold after incubation in mineralization buffer. From AFM mapping data, we inferred the morphological changes of MVs as mineralization progresses: prior to mineralization, a punctate feature, the NC, is present within MVs and this feature grows and stiffens during mineralization until it occupies most of the MV lumen. Dynamic light scattering showed a significant increase in

hydrodynamic diameter and no change in the zeta potential of hydrated MVs after incubation with Ca^{2+}. This validates that crystalline complexes, which are strongly negative relative to MVs, were forming within the lumen of MVs. These data were substantiated by transmission electron microscopy energy dispersive X-ray and Fourier transform infrared spectroscopic analyses of dried MVs, which provide evidence that the complexes increased in size, crystallinity, and Ca/P ratio within MVs during the mineralization process.

GRAPHICAL ABSTRACT

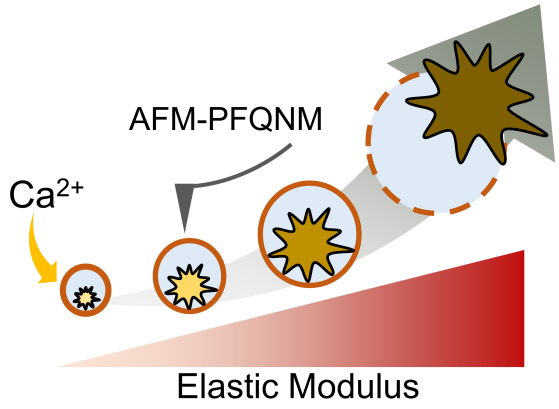

HIGHLIGHTS

- The maturation of the nucleation core was shown in hydrated matrix vesicles, whereas previous studies analyzed dried vesicle samples
- Using dynamic light scattering and zeta potential analyses, Ca-P complexes were shown to form primarily within hydrated matrix vesicles
- Peak force quantitative nanomechanical atomic force microscopy showed the morphological and physical progression of nucleation core mineralization within hydrated matrix vesicles

- Within the lumen of the matrix vesicles, the nucleation core increases in stiffness, size, and crystallinity during mineralization

Keywords: Matrix vesicles, nucleation core, mineralization, elastic modulus, atomic force microscopy

1. INTRODUCTION

Matrix vesicles (MVs) are a class of extracellular vesicles that bud from the plasma membrane of mineralization-competent cells, such as chondrocytes, osteoblasts, and odontoblasts, and play a key role in both physiologic and ectopic mineralization processes in cartilage, bone, and other vertebrate tissues [1-4]. MV-driven mineralization is considered a biphasic process: crystalline apatite minerals form inside MVs (phase I) and crystals released from MVs propagate on collagen fibrils (phase II) [1]. The ability of MVs to induce the formation of crystalline apatites resides in the presence of a nucleation core (NC) in the lumen of nascent vesicles. The first experimental evidence of the existence of the NC inside MVs was obtained approximately five decades ago by means of transmission electron microscopy (TEM) imaging and X-ray diffraction (XRD) analysis on growth plate cartilage tissues [5, 6]. Successive optimization of isolation methods enabled the routine collection of intact and biologically active MVs [7, 8]. As a result, changes in the chemical composition of the NC inside MVs following incubation in mineralizing synthetic cartilage lymph (SCL) – a buffer matched to the pH, osmolarity, and electrolyte concentrations of hypertrophic cartilage lymph – could be studied [9, 10]. Fourier transform infrared spectroscopy (FTIR), Fourier transform Raman spectroscopy, and XRD were used to confirm the presence of mixtures of calcium phosphate complexes, including apatites, attached to MVs [1-4, 11, 12]. However, it was

not unequivocally established if the apatites were formed inside or outside MVs and the physicochemical properties and function of the NC were not described. A subsequent study successfully isolated the NC by removing the MV membrane phospholipids with a detergent and revealed the morphology and chemical composition of the NC [13]. The NC is made of amorphous clusters of calcium (Ca^{2+}) and inorganic phosphate (P_i) ions stabilized by phospholipids (primarily phosphatidylserine (PS) and cholesterol) and proteins (primarily annexin A5). It has a variety of unique physical properties, including acid-lability, low solubility in aqueous buffer, and metastability, that support its role as a mediator of mineral precursor ion uptake and a nucleator for apatite precipitation [1, 13, 14]. Although these reports gave exhaustive information about the physicochemical properties of the NC and the mineral deposits formed within the MVs, dried samples were used and thus the reports could not provide indications about the location and morphology of NC nor the dynamic processes of crystal formation driven by hydrated MVs. Maintaining MVs in a hydrated state during analysis may be also crucial since the first crystals formed are surrounded by a hydration shell, which is a site of intense ion exchange between the crystals and surrounding fluids and is progressively lost during crystal maturation [15].

Recent innovations in atomic force microscope (AFM) instrumentation and probe nanofabrication have facilitated the acquisition of nanoscale-resolution topographical and quantitative nanomechanical data from samples in fluid [16-19]. Additionally, improved force control during imaging has enabled the study of fragile, hydrated biological samples with elastic moduli in the low kPa to MPa regime [16]. The nanomechanical characterization of structures enclosed by lipid bilayers has particularly benefited from these advancements: whole living cells [17-21], platelets [22], liposomes [23-25], and cell-derived vesicles, including synaptic vesicles [26] and exosomes [27, 28], have been successfully characterized with modern fluid-based AFM methods. To date, MVs and MV mimetics, such as proteoliposomes, have been exclusively imaged

in dried states using older AFM imaging methods [29, 30]. Recently, we investigated the morphology of dried MVs and the viscoelastic properties of their lumen by means of AFM phase imaging [29]. Herein, we assessed the changes in the nanomechanical and morphological properties of individual MVs triggered by the addition of Ca^{2+} to SCL buffer by using fluid-based AFM operated in peak force quantitative nanomechanical mapping mode (AFM-PFQNM). Dynamic light scattering (DLS) was used to measure the size and surface charge (zeta potential) of a population of hydrated MVs before and after the mineralization trigger and provided information about the localization of the formed crystalline complexes. These analyses were complemented by assessing the changes in the chemical composition of the vesicle lumen by means of transmission electron microscopy energy dispersive X-ray spectroscopy (TEM-EDX) and FTIR analyses on dried MV samples. AFM-PFQNM has enabled us to quantitate the physical progression of MV-driven mineralization at a single vesicle level under biologically-relevant conditions.

2. EXPERIMENTAL METHODS

2.1. Matrix vesicle isolation

MVs were isolated from 17-day-old chicken embryos by a collagenase digestion method [8]. Growth plates and epiphyseal cartilages were cut in 1-3 mm thick slices and washed in ice cold SCL buffer (1.42 mM NaH_2PO_4·H2O, 1.83 mM $NaHCO_3$, 12.7 mM KCl, 0.57 mM $MgCl_2$, 5.55 mM D-glucose, 63.5 mM sucrose, 16.5 mM TES, 100 mM NaCl, and 0.57 mM Na_2SO_4) diluted 1:4 in water. The slices were incubated in SCL containing 1 mM $CaCl_2$·H_2O and collagenase type I A (200 U/g tissue, Sigma-Aldrich, St. Louis, MO) at 37ºC for 3 h, filtered and centrifuged at 13,000 × *g* for 20 min at 4ºC. The pellet was discarded, and the supernatant was centrifuged for 60 min at 80,000 × *g* and 4ºC. Next, the supernatant was discarded, and the pellet was washed with

SCL to remove the calcium and collagenase. The MV-enriched pellet was suspended in SCL and the total protein concentration of each sample fraction was 0.5–1.8 mg/ml as determined by a Bradford protein assay kit (Thermo Fisher Scientific, Waltham, MA) performed at 37ºC with absorbance measured at 562 nm.

For all experiments, SCL buffer supplemented with 2 mM $CaCl_2$ was used as a mineralization trigger. This recapitulates the Ca^{2+} concentration found in the hypertrophic epiphyseal cartilage fluid of chickens [10] and is the concentration required for the maximal rate of uptake into MV mimetic proteoliposomes [31].

2.2. Turbidity measurement

MVs (~250 µg total proteins/ml) were dispersed in SCL containing 3.42 mM $NaH_2PO_4 \cdot H_2O$ and the turbidity was measured at 340 nm for 200 min at 37ºC with and without 2 mM Ca^{2+} using a SpectraMax M5e Multi-Detection microtiter plate reader (Molecular Devices, San Jose, CA) and served as an indicator for mineral formation. Three independent measurements were performed.

2.3. Tissue-nonspecific alkaline phosphatase enzymatic activity

The activity of tissue-nonspecific alkaline phosphatase (TNAP, UniProtKB Q92058) present in the MV membrane was measured using the ALP Yellow *para*-nitrophenyl phosphate (pNPP) Liquid Substrate System for ELISA (Sigma-Aldrich) [32]. Aliquots (10 µl) of MVs (~20 µg total protein/ml) were mixed with 200 µl of p-NPP into a 96-well plate at 37ºC for 5 min, and the absorbance was recorded at 405 nm for 200 min using a microtiter plate reader. Three independent measurements were performed. TNAP activity was calculated as the number of enzyme units (U) per mg of total protein (1 U corresponds to 1 µmol of pNPP hydrolyzed per min).

2.4. Dynamic light scattering

MVs were incubated at 37ºC in SCL with and without 2 mM Ca^{2+} for 24 h, diluted 1:10 in their respective SCL buffers and gently centrifuged to pellet any large debris. The supernatants were collected and the Z-average hydrodynamic diameter and zeta potential of hydrated MVs were measured via DLS on a Zetasizer Nano ZSP instrument (Malvern Panalytical Ltd, Malvern, United Kingdom). To minimize electrode degradation during zeta potential measurements, each MV sample was directly injected into the optical window of a DTS1070 folded capillary zeta cell (Malvern Panalytical Ltd) prefilled with sample-matched SCL buffer.

2.5. Peak force quantitative nanomechanical AFM

AFM images were acquired in Peakforce Tapping Mode with Peakforce-HiRs-F-A probes (nominal spring constant = 0.35 N/m; nominal end radius = 1 nm; low profile silicon nitride cantilever and etched pyramidal silicon crystal tip) and an Icon Scanning Head on a Dimension Fastscan System (Bruker Nano Surfaces, Santa Barbara, CA). We chose a sharp AFM probe with low spring constant, low hydrodynamic drag, and precise force control so as to maintain low indentation volume relative to vesicle volume during imaging. For the more deformable MV sample without added Ca^{2+}, the average percent volume indented during each force curve was 0.21–0.29% and the 95^{th} percentile of indentation was 0.68–0.92%. As described in a recent study and validated empirically during our AFM parameter optimization, the apparent elastic modulus of liposomes and other membrane-bound particles increases when an indenter generates an osmotic restoring force resulting from compression of the fluid volume enclosed within the membrane [33]. Probe selection and imaging parameter optimization is critical to limit compression of the vesicles.

Each probe was individually calibrated in accordance with current best practices: deflection sensitivity was calibrated with a minimum of 30 force curves with 800 pN applied force on a clean glass surface after 20 min thermal equilibration with sample-matched buffer and the cantilever spring constant (k) was calibrated using a thermal tune method with appropriate correcting factors [34-39]. The probes had measured spring constants in the range of 0.15–0.17 N/m. All buffers were prefiltered through sterile 0.1 μm hydrophilic polyvinylidene fluoride membranes. The calibration force was set four times greater than the imaging force to minimize error in the deflection sensitivity calculation and to increase the end radius of the probe to approximately 8 nm (**Figure S1**). This prevented puncturing the MV particles during imaging. For sharp probes, the wear during calibration is critical to ensure a consistent tip size and shape throughout each experiment. After the experiments, the spherical end radius and vertical half angle of the probes was measured using a Helios Nanolab 660 DualBeam (FEI Materials & Structural Analysis Division, Hillsboro, OR) focused ion beam and scanning electron microscope (SEM) for indentation analysis (**Supplementary Methods** and **Figure S1**). SEM images showed that the probes had end radii in the 7–9 nm range and that at least the terminal 150 nm end of the probes were closely conical in geometry (**Figure S1**). This is significantly greater than the maximum observed MV indentation (80 nm), so conical indentation models should theoretically apply.

Sample substrate was prepared by incubating 0.01% aqueous poly-L-ornithine (PLO; Sigma-Aldrich) at 21ºC on freshly cleaved mica discs (Ted Pella, Redding, CA), rinsing with water, and drying under vacuum. MVs were incubated in SCL with and without 2 mM Ca^{2+} at 37ºC for 24 h, diluted 1:10 in their respective SCL buffers and gently centrifuged to remove large debris. Twenty-five microliters of the supernatant were then incubated on a PLO-mica surface at 21ºC for 2 h, rinsed with sample-matched SCL buffer, thermally equilibrated on the AFM under a column of buffer for at least 20 min, and imaged at 21ºC in buffer.

Individual MVs were documented with 500 nm scans at 0.5 Hz and 256×256 resolution with 200 pN applied peak force and 75 nm peak force amplitude in a single scan direction and all force curves were collected in a peak force capture file (PFC). The elastic moduli of MVs were computed in Nanoscope Analysis 1.9 (Bruker Nano Surfaces) from the PFC using the Briscoe-Sebastian-Adams (BSA) conico-spherical indenter model [40]. The BSA model was chosen over conventional models because the average MV indentation depth was not sufficiently large for the Sneddon conical indenter model [41] nor sufficiently small for the Hertzian spherical indenter model [42] to apply (**Figure S2**). Furthermore, the BSA model best fit the trajectory of MV force curves acquired from various indentation depths (**Figure S3**). The loading (approach) and unloading (retract) portions of the force curves were synchronized using the mica substrate as a hard reference, all force curves were baseline fitted to the initial 10–50% of the loading curve tip-sample separation distance, and the BSA indenter model was fitted to the contact region of the loading curve corresponding to 15–80% of the peak applied force. Unloading curves are typically used for calculating elastic moduli [43-45], but strong adhesion was observed in the unloading curves of >85% of the measured MVs. The average elastic modulus calculated from the unloading curves was 30% greater than the value calculated from the loading curves (**Figure S4**). Minimal hysteresis between the loading and unloading curves was observed, which indicates minimal viscoelastic dissipation of energy, so the majority of this difference can be attributed to adhesion. Low hysteresis also enabled us to approximate MVs as elastic. Since the BSA model does not account for adhesion and loading curves can be reasonably employed for elastic materials [40], we chose to use the loading curves for our analysis as they provided a more accurate fit. To minimize artifacts from the substrate-to-MV transition, force curves from the highly sloped edges of each MV were omitted from analysis. A minimum of 235 force curves about the region of maximum height of each MV were analyzed. Elastic modulus values were calculated from the loading curves

assuming a 0.5 Poisson's ratio [46-48] and averaged to yield the elastic modulus of each MV. This approach was also applied to unloading curves and to the average of loading and unloading curves (**Figure S4**). The elastic modulus describes the resistance to deformation when an elastic material is subject to an applied force; a higher elastic modulus implies a stiffer MV and a lower elastic modulus implies a softer MV.

2.6. TEM-EDX and FTIR spectroscopy

MVs were incubated at 37ºC in SCL with and without 2 mM Ca^{2+} for 24 h and briefly centrifuged at 2000 × *g*. The supernatants were collected and dropped onto a Formvar-carbon 300 mesh Ni grid to record TEM images and EDX spectra by a JEM-1400 microscope (JEOL USA, Inc., Peabody, MA) equipped with an INCA energy dispersive X-ray microanalysis system (Oxford Instruments plc, Abingdon, United Kingdom) and a 11 Megapixel MORADA G2 camera (Olympus Soft Imaging Solutions GmbH, Münster, Germany). The MVs were counterstained with 2.5% (by volume) uranyl acetate in EtOH, washed in 50% EtOH (by volume) and deionized water, and then dried [32]. The spectral and compositional analyses were carried out on point measurements of elements in TEM images and the Ca/P ratio calculated for each sample. After 24 h of incubation at 37ºC in SCL with and without 2 mM Ca^{2+}, MVs were dried and dropped onto a diamond attenuated total reflection cell to record FTIR spectra on a Nicolet iS10 system (Thermo Fisher Scientific). Six infrared spectra from three independent MV samples were measured at two distinct locations and averaged.

2.7. Statistical analyses

DLS and AFM data are presented as mean ± standard deviation and all other data are presented as mean ± standard error. Statistical significance was assessed with unpaired, two-tailed t-tests (n.s. = not significant; * $p < 0.05$; ** $p < 0.01$ in all figures).

3. RESULTS

3.1. Turbidity analysis and TNAP activity assay to assess MV functionality

The functionality of MVs isolated by the collagenase digestion method were validated by measuring the changes in turbidity (**Figure 1A**) and TNAP activity (**Figure 1B**) after incubation of MVs in SCL devoid of Ca^{2+} (MV Neat) and supplemented with 2 mM Ca^{2+} (MV+Ca^{2+}). Within 200 min of incubation, the turbidity of MVs in the presence of Ca^{2+} increased, but remained low in the absence of Ca^{2+} (**Figure 1A**), which is consistent with functional MVs [8, 49]. Control experiments showed that the addition of Ca^{2+} to SCL did not induce any changes in turbidity (**Figure 1A**). TNAP activity present in the MV membrane was approximately 35 U/mg under non-mineralizing conditions and showed a significant decrease after 200 min of incubation with Ca^{2+} (**Figure 1B**), which is also consistent with functional MVs [50, 51].

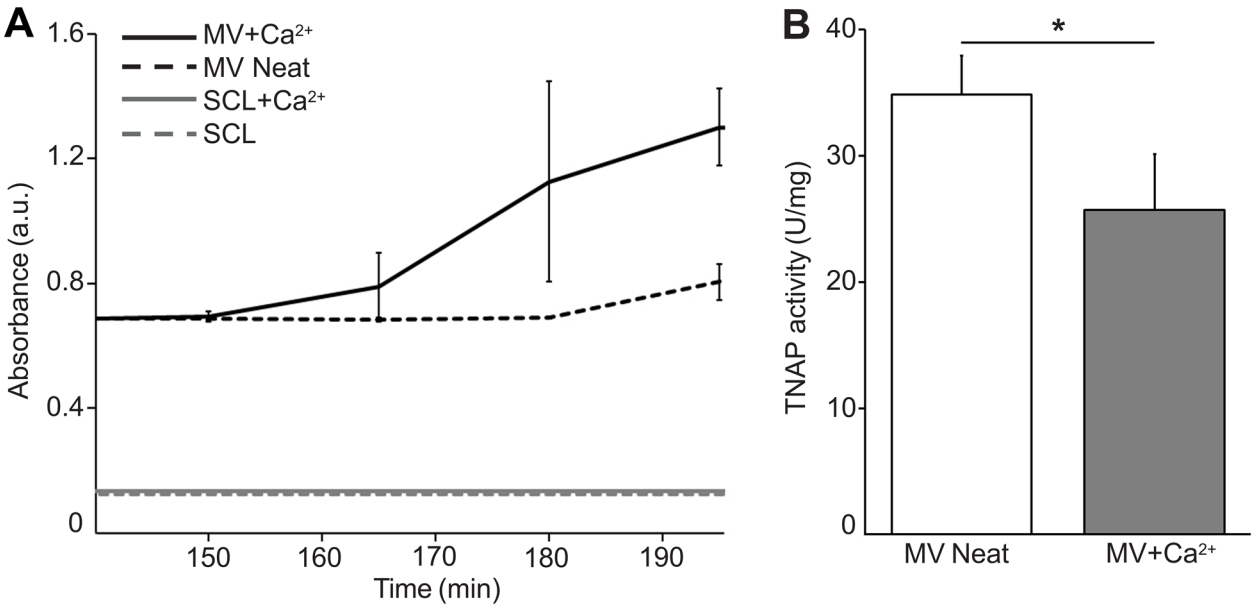

Figure 1. Characterization of MV functionality by turbidity and TNAP activity analyses. (A) Turbidity time course data from MV solutions with ($MV+Ca^{2+}$) and without (MV Neat) Ca^{2+}. SCL buffer with ($SCL+Ca^{2+}$) and without Ca^{2+} (SCL) were used as negative controls. (B) TNAP activity assay of MVs before Ca^{2+} addition (MV Neat) and 200 min after addition ($MV+Ca^{2+}$).

3.2. DLS analysis of hydrated MVs to determine vesicle size and zeta potential

Hydrated MVs in SCL were analyzed by DLS to acquire bulk measurements of MV diameter and zeta potential. DLS analysis showed that incubation with 2 mM Ca^{2+} led to a significant increase in the hydrodynamic diameter of the MV population from 160 ± 40 nm (polydispersity index (PDI) = 0.196) to 190 ± 50 nm (PDI = 0.285) (**Figure 2A**). However, the zeta potential did not show a significant difference before (-8.8 ± 0.8 mV) and after (-9 ± 1 mV) incubation with Ca^{2+} (**Figure 2B**).

3.3. AFM-PFQNM analyses of individual hydrated MVs to compute elastic modulus

MVs were immersed in SCL with or without Ca^{2+} for 24 h, immobilized on PLO-mica substrates, and individual vesicles were imaged in buffer by AFM-PFQNM. Since the zeta potential data showed that MVs are negatively charged, we chose a positively charged PLO surface to which MVs were electrostatically adsorbed for the AFM-PFQNM studies. The elastic modulus of individual MVs significantly increased from 230 ± 90 kPa for MV Neat to 900 ± 700 kPa for MV+Ca^{2+} (**Figure 2C**). Representative modulus maps illustrate this increase (**Figure 2D**).

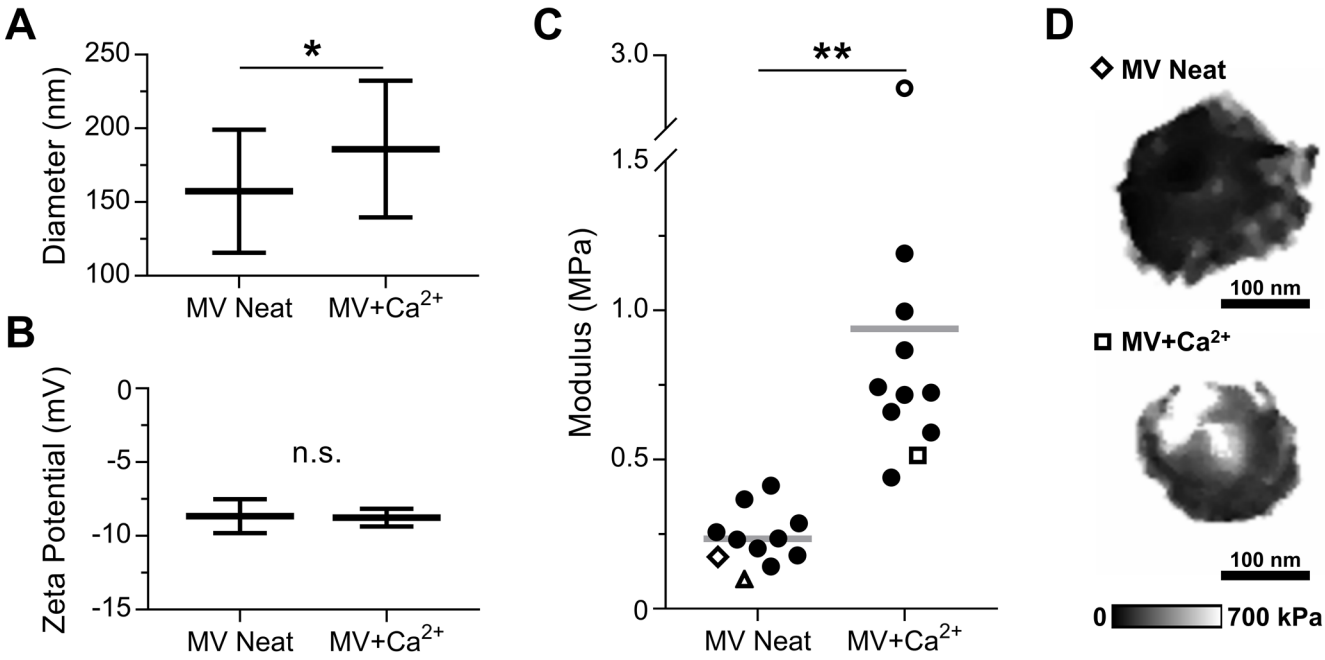

Figure 2. Characterization of NC mineralization by DLS and AFM-PFQNM measurements of hydrated MVs. MVs were incubated in SCL devoid of Ca^{2+} (MV Neat) or supplemented with 2 mM Ca^{2+} (MV+Ca^{2+}) for 24 h. (A) Hydrodynamic diameter (n = 25 measurements per group) and (B) zeta potential (n = 10 measurements per group) of MV samples. (C) Elastic modulus data calculated from AFM micrographs of individual vesicles acquired in PFQNM mode (n = 11 vesicles per group, data calculated from loading curves). Each marker corresponds to the average elastic modulus of a single MV and the horizontal bar is the mean of the group. Hollow markers

correspond to individual MVs shown here and in Figure 3. (D) Modulus maps of representative individual vesicles.

3.4. AFM mapping to evaluate morphology of individual hydrated MVs

Using AFM-PFQNM, high resolution morphological data was also acquired. In absence of Ca^{2+}, MVs appeared as highly deformable spheroidal particles with one well-defined peak on the surface (**Figure 3A**, panels i–ii). Greater deformation was observed on and around these peaks relative to surrounding regions of the vesicles (**Figure S5**, panels i–ii). Slight inward puckering of the membrane surrounding the peak was observed in the cross sections of most of the MV Neat vesicles but was less evident or absent in the MV+Ca^{2+} vesicles (**Figure 3B**, panels i-ii *versus* iii-iv). After 24 h incubation with Ca^{2+}, MV+Ca^{2+} vesicles exhibited higher elastic moduli (lower deformation) compared to the MV Neat vesicles (**Figure S5**, panels iii–iv). Additionally, a well-defined peak was not visible in all of the vesicles (**Figure 3B**, panel iv). When a peak was observed in a MV+Ca^{2+} vesicle, it showed greater elastic modulus (lower deformation) relative to surrounding regions of the vesicle (**Figure S5**, panel iii). MV+Ca^{2+} vesicles without a defined peak exhibited a very high elastic modulus (extremely low deformation) relative to all other measured MVs (**Figure 3B**, panel iv, and **Figure S5**, panel iv).

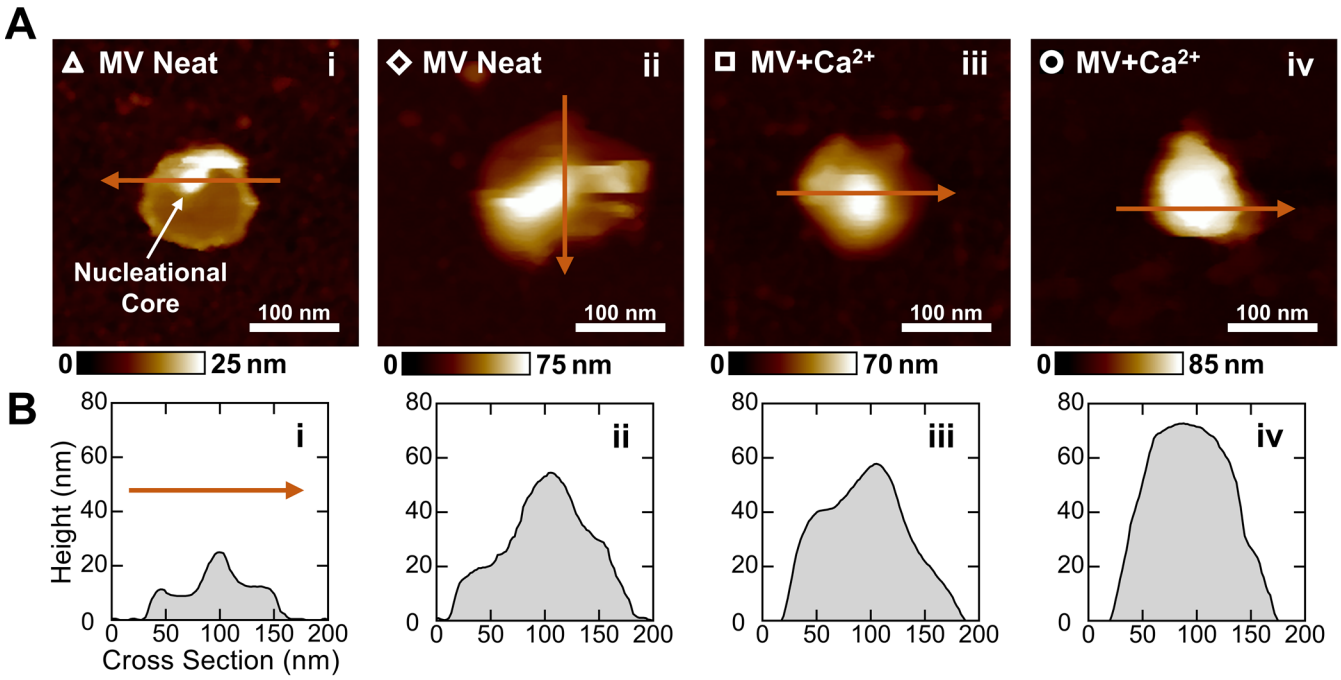

Figure 3. Morphological characterization of different MVs before and after mineralization by AFM-PFQNM. (A) Height maps of representative MVs arranged in the order that mineralization is expected to proceed. The hollow markers correspond to the elastic modulus data points in Figure 2C. An intense peak believed to be the NC is indicated in panel i. (B) Two-dimensional cross sections of MVs taken across the maximum height of each vesicle. The arrows in (A) show the direction of each cross-sectional measurement.

3.5. TEM-EDX measurements of dried MVs to assess extent of mineralization

MVs were incubated in SCL devoid of or supplemented with 2 mM Ca^{2+} at 37ºC for 24 h and dried. TEM images showed distorted and aggregated discoidal particles with diameters of approximately 100–300 nm (**Figure 4A**), which is consistent with previous TEM imaging of MVs [4, 5]. These electron micrographs orthogonally confirm the presence and activity of MVs under both experimental conditions. In the absence of Ca^{2+}, ~20% of the MVs were devoid of electron dense material, whereas the remaining MVs exhibited either electron dense deposits anchored to

the inner leaflet of the membrane (~40%) or were completely filled with electron dense material (~40%) (**Figures 4A** and **B**). After incubation with Ca^{2+}, the frequency of completely filled MVs increased to more than 80%, which suggests the sequestration of Ca^{2+} and P_i in the MV lumen and the maturation of the NC (**Figures 4A** and **B**). TEM-EDX analysis showed that the Ca/P ratio of MVs significantly increased from ~0.1 to ~0.6 after incubation with Ca^{2+} (**Figure 4C**).

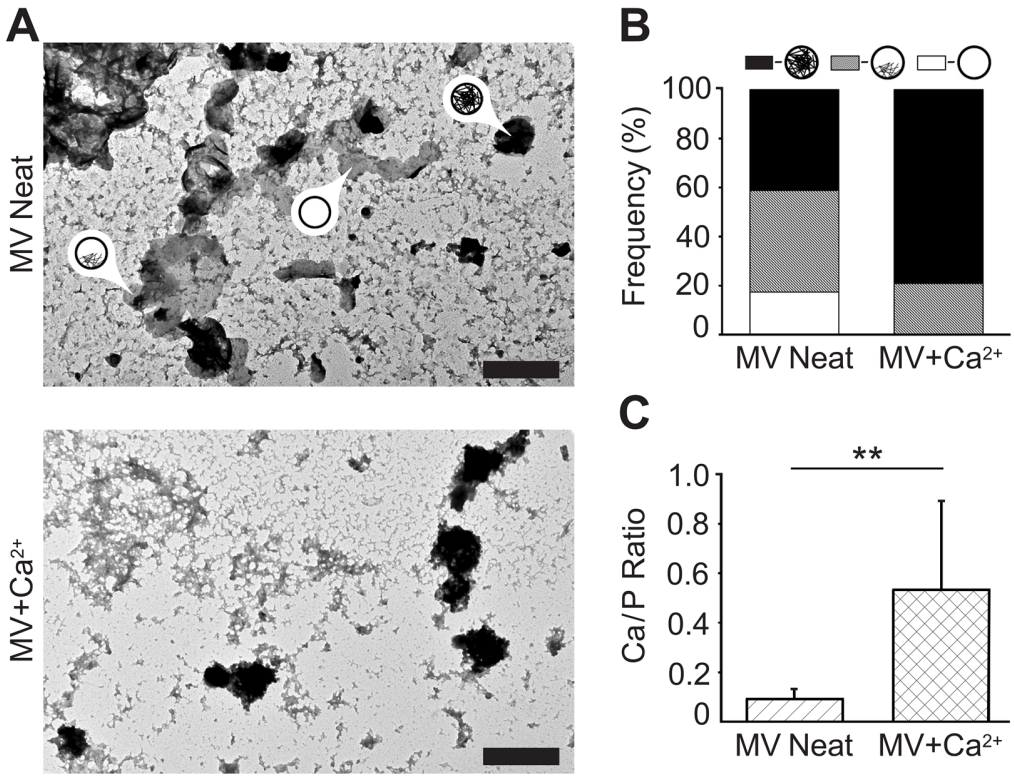

Figure 4. Characterization of NC mineralization by TEM-EDX analyses of dried MVs. MVs were incubated in SCL devoid of Ca^{2+} (MV Neat) or supplemented with 2 mM Ca^{2+} (MV+Ca^{2+}) for 24 h, then dried and analyzed by means of TEM-EDX. (A) TEM images (scale bars are 500 nm) of MVs devoid of, partially filled with, and fully filled with mineral deposits (arrows with labels). (B) Frequency of MVs devoid of (white area), partially filled with (grey area), and fully filled with (black area) mineral deposits. (C) The Ca/P ratio of mineral deposits found in MVs incubated in SCL devoid of Ca^{2+} (MV Neat, hatched area) or supplemented with 2 mM Ca^{2+} (MV+Ca^{2+}, crosshatched area) as measured by TEM-EDX.

3.6. FTIR measurements of dried MVs to determine the presence and crystallinity of contained apatites

The FTIR spectrum of the MV+Ca^{2+} sample showed characteristic apatite bands located at 633, 600, and 559 cm^{-1} (**Figure 5**) [9]. In contrast, the spectrum of the MV Neat sample showed only a weak band at 600 cm^{-1}, which suggests that there is only a small amount of apatite material present within these vesicles. The apatite bands at 1090, 1022, and 962 cm^{-1} were not clearly visible in the FTIR spectra of either sample because of overlap with a broad absorption band at 1043 cm^{-1} (P-O-C) that is characteristic of the vesicle membrane phospholipids. Therefore, the MV Neat spectrum was subtracted from the MV+Ca^{2+} spectrum to negate the background contribution of phospholipids, phosphate groups, and other MV components. After amplification by a factor of 4, the background-subtracted MV+Ca^{2+} spectrum displayed the characteristic absorption bands seen in the crystalline hydroxyapatite control (**Figure 5**).

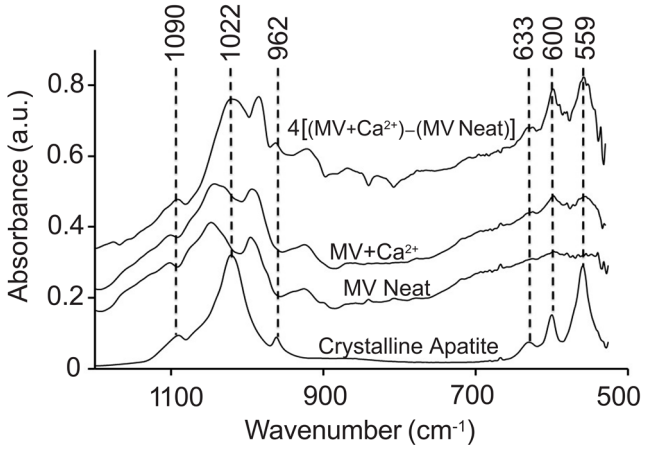

Figure 5. Characterization of NC mineralization by FTIR measurements of dried MVs. MVs were incubated in SCL devoid of Ca^{2+} (MV Neat) or supplemented with 2 mM Ca^{2+} (MV+Ca^{2+}) for 24 h, then dried and analyzed by means of FTIR. The top trace is the spectrum for MV+Ca^{2+} after background subtraction of the MV Neat sample and subsequent amplification by a factor of four to better resolve the peaks. The spectrum of crystalline hydroxyapatite is reported as a control. All FTIR spectra were averaged from at least three independent samples.

4. DISCUSSION

According to a biphasic model for MV-driven mineralization, the ability of MVs to induce the formation of crystalline apatites resides in the presence of the nucleation core (NC) in the lumen of nascent vesicles [1]. The formation of the NC is thought to begin in the perimeter of mineral-competent cells with complexes of Ca^{2+}, P_i, and PS (PS-CPLX) formed on the inner leaflet of the plasma membrane and incorporated into MVs when they bud off from the cells [1, 52]. Following MV release from cells, Ca^{2+} and P_i adsorb onto the vesicle membrane and move into the lumen through Annexin V [30, 31, 53, 54] and Na-P_i transporters [29], respectively. P_i can be also directly produced intravesicularly by PHOSPHO1 and ATPases [29]. At this stage, amorphous clusters of Ca^{2+} and P_i ions (ACP) are rapidly formed in the vesicle lumen. These clusters are the major component of the NC and mediate further Ca^{2+} and P_i uptake by MVs (induction phase) [13]. When sufficient Ca^{2+} and P_i have accumulated within the vesicle, Ca^{2+}-P_i minerals begin to convert into ordered apatite structures. Finally, apatite crystals penetrate the vesicles membrane assisted by the action of phospholipases and are exposed to the extravesicular environment where they form mineral clusters and interact with collagen fibers in the extracellular matrix [1, 2]. This model has been substantiated by means of imaging (TEM and AFM) and spectroscopic (FTIR, FT-Raman, and XRD) approaches on growth plate cartilage tissues, collagenase-released MVs, and isolated NC [1-4, 11-13]. AFM operated in both topography and phase imaging modes in air was recently used by our research group to assess the surface morphology and lumen content of dried MVs [29]. Phase images validated the presence of the NC in the vesicle lumen and provided qualitative information of the differences in the viscoelastic properties between the inorganic phase of the NC (the ACP complexes) and the surrounding regions rich in lipids and proteins. Although these reports gave exhaustive information about the physicochemical properties of the first mineral phase (the NC) and the mineral deposits formed in the MVs at the end of the induction phase, they

employed dried samples and cannot provide indications about the dynamic processes of crystal formation inside MVs in a hydrated state. Additionally, these studies did not unambiguously show that apatites were not also formed outside of the MVs.

Herein, we utilized recent innovations in AFM instrumentation, software, and probe nanofabrication to acquire topographical and quantitative nanomechanical characteristics of individual MVs in fluid at nanoscale resolution [16-28, 41]. By using AFM-PFQNM, we provided direct experimental evidence of the changes in the morphology and physical properties of the NC induced by the accumulation of Ca^{2+} in hydrated MVs. These data showed that MVs immersed in a non-mineralizing buffer (SCL devoid of Ca^{2+}) were spheroidal with an elastic modulus of 230 ± 90 kPa and a well-defined surface peak. Addition of a mineralization trigger led to more than a four-fold increase in the vesicle elastic modulus and the obfuscation or disappearance of the well-defined surface peak. This punctate feature is the NC in a relatively immature, less-mineralized state. As it further mineralizes and matures in the presence of Ca^{2+}, it grows and occupies much of the MV lumen, loses its punctate appearance, and the elastic modulus greatly increases. This suggests the NC matures from an amorphous phase (lower elastic modulus) to a more-crystalline phase (higher elastic modulus). Since the isolated MVs undoubtedly had some Ca^{2+} exposure within the chicken embryos, we expect that the samples in both non-mineralizing and mineralizing conditions contain a distribution of MVs at various stages of mineralization. This enabled us to arrange, as determined by modulus and morphology, the different MVs of **Figure 3** in the sequence by which we expect normal mineralization to proceed. Despite similarities in morphology, particularly between the vesicles in panels ii and iii (**Figure 3**), the elastic moduli of these vesicles are very different (**Figure 2**, hollow markers). The increase in size and elastic modulus of MVs after addition of Ca^{2+} supports the prevailing hypothesis that Ca^{2+}-P_i complexes grow within MVs until they are released [4]. This hypothesis was further supported by DLS data showing that the

hydrodynamic diameter of MVs significantly increased after incubation with Ca^{2+}, but that the zeta potential was unchanged (**Figure 2**). Since Ca^{2+}-P_i complexes typically exhibit a highly negative zeta potential (< –14 mV) [55] and zeta potential is a function of surface charge [56, 57], these data suggest that the complexes form inside of the MVs, which causes the vesicles to swell in size. If the Ca^{2+}-P_i complexes were forming on the outer membrane leaflet of the MVs, then we would expect a decrease in the zeta potential of the MV+Ca^{2+} sample relative to the MV Neat sample, which was not observed.

The functionality of MVs under non-mineralizing conditions (MV Neat) was validated by showing enzymatic activity of TNAP in the MV membrane. Several lipids and proteins of the MV membrane mediate the interactions of MVs with the ECM and regulate both phases of MV-mediated mineralization [54]. Among these proteins, TNAP, when reconstituted in MV-biomimetic proteoliposomes, showed the ability to induce mineralization even in the absence of an intraluminal mineral nucleators [58]. A significant decrease in TNAP activity was observed in the presence of calcium (MV+Ca^{2+}) (**Figure 1B**), which is consistent with functional MVs [50]. The Mg^{2+} co-factor of TNAP can be substituted by Ca^{2+}, thus modulating enzymatic activity of TNAP. During skeletal mineralization, the building Ca^{2+} gradient first activates TNAP, but then gradually inactivates it at high Ca^{2+} concentrations and toward completion of mineralization [50, 51].

The DLS and AFM-PFQNM data were substantiated and complemented by TEM-EDX (**Figure 4**) and FTIR (**Figure 5**) analyses of dried vesicles. These data showed that MVs dispersed in SCL devoid of Ca^{2+} were partially filled with electron dense material, which was mostly anchored to the inner leaflet of the vesicles, and do not display the distinct FTIR spectroscopic features of hydroxyapatite crystals. This validates the presence of a NC composed of amorphous Ca^{2+}-P_i complexes in the MV lumen. After incubation with Ca^{2+}, the vesicles increased in size, became

filled with electron dense material, and showed a significant increase in the Ca/P ratio of the contained material. Additionally, the background-corrected MV+Ca^{2+} FTIR spectrum showed distinct orthophosphate (P-O) absorption bands in the 650–550 cm^{-1} and 1100–950 cm^{-1} regions, which are characteristic of hydroxyapatite crystals. Collectively, these results are consistent with our conclusions from DLS and AFM-PFQNM and suggest that, after incubation with Ca^{2+}, the amorphous NC matured into larger and more crystalline Ca^{2+}-P_i complexes.

5. CONCLUSIONS

We showed the maturation of the NC inside the MVs by measuring the nanomechanical properties of individual vesicles – and their contained mineral deposits – by AFM-PFQNM. Supporting evidence of this maturation was provided by various physicochemical characterization techniques. Additionally, we discovered morphological differences of MVs at various stages of mineralization and applied zeta potential data to confirm that the Ca^{2+}-P_i complexes are indeed forming within the MVs. The advantage of this approach based on DLS and AFM-PFQNM methods is that the MVs remained hydrated and functional within physiologically relevant conditions. In future studies, we plan to dynamically track the mineralization and mineral release process by continuous AFM-PFQNM imaging of individual MVs. We envision that this approach will help detect any morphological or kinetic differences in NC maturation of MVs and related vesicles released during both physiological and pathological processes. This has relevance to bone tissue regeneration; the formation of atherosclerotic deposits, arterial calcifications, breast microcalcifications, and osteoarthritic calcifications; the growth and metastasis of osteo- and chondrosarcomas; and the mineral loss associated with osteoporosis.

ASSOCIATED CONTENT

Supporting Information

Supporting Methods; Figures S1: Geometric characterization of atomic force microscopy probes; Figure S2: Indentation models for elastic modulus determination; Figure S3: Indentation model fitting to force curves acquired from matrix vesicles; Figure S4: Elastic moduli of matrix vesicles from loading, unloading, and averaged curves; Figure S5: Three-dimensional renderings of matrix vesicles with overlaid deformation maps.

AUTHOR INFORMATION

Author Contributions

Study design: SP, RB, PC, CF, SE, JLM, and MB. Experimentation, method development, and data collection: JSP, ASK, LB, SM, MC, and MB. Data analysis and interpretation: JSP, ASK, RB, MB, AMSS, AM, AGE, JLM and MB. Drafting and revising manuscript: JSP, ASK, SP, RB, PC, NR, DM, CF, SE, JLM and MB.

Funding Sources

This work was supported by grant NanOArt from the University of Rome Tor Vergata, grant DE128890 from the National Institute of Dental and Craniofacial Research (NICDR), grant T32EB009380 from the National Institute of Biomedical Imaging and Bioengineering (NIBIB), grants 2016/21236-0 and 2014/11941-3 from FAPESP, 167497/2017-0 from CNPq, Coordenação de Aperfeiçoamento de Pessoal de Nível Superior - Brasil (CAPES) - Finance Code 001, grant support from the Polish Academy of Sciences, the Hubert Curien Partnership Program between Governments of the Republic of Poland and the Republic of France POLONIUM 2018/2019 (project no 1/A/1), and grant 2016/23/N/NZ4/03313 from the Polish National Science Centre.

Notes

The authors report no conflicts of interest.

ACKNOWLEDGMENTS

We thank Dr. Jian Liang for AFM technical advice. Scanning electron microscopy was performed at the Multi-scale Microscopy Core (MMC) with technical support from the Oregon Health & Science University (OHSU)-FEI Living Lab and the OHSU Center for Spatial Systems Biomedicine (OCSSB).

ABBREVIATIONS

AFM-PFQNM, atomic force microscopy peak force quantitative nanomechanical property mapping; BSA, Briscoe-Sebastian-Adams; DLS, dynamic light scattering; FTIR, Fourier transform infrared; MV, matrix vesicle; MV Neat, matrix vesicles suspended in synthetic cartilage lymph without calcium chloride; MV+Ca^{2+}, matrix vesicles suspended in synthetic cartilage lymph with calcium chloride; NC, nucleation core; PDI, polydispersity index; PFC, peak force capture; P_i, inorganic phosphate; PLO, poly-L-ornithine; PS, phosphatidylserine; SCL, synthetic cartilage lymph buffer; SEM, scanning electron microscope; TEM-EDX, transmission electron microscopy energy dispersive X-ray; TNAP, tissue-nonspecific alkaline phosphatase; XRD, X-ray diffraction.

REFERENCES

[1] R.E. Wuthier, G.F. Lipscomb, Matrix vesicles: structure, composition, formation and function in calcification, Front. Biosci. (Landmark Ed.) 16(1) (2011) 2812-902. https://doi.org/10.2741/3887.

[2] H.C. Anderson, Matrix vesicles and calcification, Curr. Rheumatol. Rep. 5(3) (2003) 222-6. https://doi.org/10.1007/s11926-003-0071-z.

[3] E.E. Golub, Biomineralization and matrix vesicles in biology and pathology, Semin. Immunopathol. 33(5) (2011) 409-17. https://doi.org/10.1007/s00281-010-0230-z.

[4] M. Bottini, S. Mebarek, K.L. Anderson, A. Strzelecka-Kiliszek, L. Bozycki, A.M.S. Simao, M. Bolean, P. Ciancaglini, J.B. Pikula, S. Pikula, D. Magne, N. Volkmann, D. Hanein, J.L. Millan, R. Buchet, Matrix vesicles from chondrocytes and osteoblasts: Their biogenesis, properties, functions and biomimetic models, Biochim. Biophys. Acta. Gen. Subj. 1862(3) (2018) 532-546. https://doi.org/10.1016/j.bbagen.2017.11.005.

[5] H.C. Anderson, Vesicles associated with calcification in the matrix of epiphyseal cartilage, J. Cell Biol. 41(1) (1969) 59-72. https://doi.org/10.1083/jcb.41.1.59.

[6] A.L. Arsenault, E.B. Hunziker, Electron microscopic analysis of mineral deposits in the calcifying epiphyseal growth plate, Calcif. Tissue. Int. 42(2) (1988) 119-26. https://doi.org/10.1007/bf02556344.

[7] L.N. Wu, T. Yoshimori, B.R. Genge, G.R. Sauer, T. Kirsch, Y. Ishikawa, R.E. Wuthier, Characterization of the nucleational core complex responsible for mineral induction by growth plate cartilage matrix vesicles, Journal of Biological Chemistry 268(33) (1993) 25084-94.

[8] R. Buchet, S. Pikula, D. Magne, S. Mebarek, Isolation and characteristics of matrix vesicles, Methods Mol. Biol. 1053 (2013) 115–24. https://doi.org/10.1007/978-1-62703-562-0_7.

[9] G.R. Sauer, R.E. Wuthier, Fourier transform infrared characterization of mineral phases formed during induction of mineralization by collagenase-released matrix vesicles in vitro, Journal of Biological Chemistry 263(27) (1988) 13718-24.

[10] R.E. Wuthier, Electrolytes of isolated epiphyseal chondrocytes, matrix vesicles, and extracellular fluid, Calcified Tissue Research 23(1) (1977) 125-133. https://doi.org/10.1007/bf02012777.

[11] R. Garimella, X. Bi, H.C. Anderson, N.P. Camacho, Nature of phosphate substrate as a major determinant of mineral type formed in matrix vesicle-mediated in vitro mineralization: An FTIR imaging study, Bone 38(6) (2006) 811-7. https://doi.org/10.1016/j.bone.2005.11.027.

[12] G.R. Sauer, W.B. Zunic, J.R. Durig, R.E. Wuthier, Fourier transform Raman spectroscopy of synthetic and biological calcium phosphates, Calcif. Tissue Int. 54(5) (1994) 414-20. https://doi.org/10.1007/BF00305529.

[13] L.N. Wu, B.R. Genge, D.G. Dunkelberger, R.Z. LeGeros, B. Concannon, R.E. Wuthier, Physicochemical characterization of the nucleational core of matrix vesicles, Journal of Biological Chemistry 272(7) (1997) 4404-11. https://doi.org/10.1074/jbc.272.7.4404.

[14] T.C. Register, F.M. McLean, M.G. Low, R.E. Wuthier, Roles of alkaline phosphatase and labile internal mineral in matrix vesicle-mediated calcification. Effect of selective release of membrane-bound alkaline phosphatase and treatment with isosmotic pH 6 buffer, Journal of Biological Chemistry 261(20) (1986) 9354-60.

[15] D. Magne, P. Weiss, J.M. Bouler, O. Laboux, G. Daculsi, Study of the maturation of the organic (type I collagen) and mineral (nonstoichiometric apatite) constituents of a calcified tissue (dentin) as a function of location: A Fourier transform infrared microspectroscopic investigation, J. Bone Miner. Res. 16(4) (2001) 750-757. https://doi.org/10.1359/jbmr.2001.16.4.750.

[16] J. Adamcik, A. Berquand, R. Mezzenga, Single-step direct measurement of amyloid fibrils stiffness by peak force quantitative nanomechanical atomic force microscopy, Appl. Phys. Lett. 98(19) (2011) 193701. https://doi.org/10.1063/1.3589369.

[17] E.M. Darling, Force scanning: a rapid, high-resolution approach for spatial mechanical property mapping, Nanotechnology 22(17) (2011) 175707. https://doi.org/10.1088/0957-4484/22/17/175707.

[18] A.X. Cartagena-Rivera, W.H. Wang, R.L. Geahlen, A. Raman, Fast, multi-frequency, and quantitative nanomechanical mapping of live cells using the atomic force microscope, Sci. Rep. 5 (2015) 11692. https://doi.org/10.1038/srep11692.

[19] A. Raman, S. Trigueros, A. Cartagena, A.P.Z. Stevenson, M. Susilo, E. Nauman, S.A. Contera, Mapping nanomechanical properties of live cells using multi-harmonic atomic force microscopy, Nat. Nanotechnol. 6(12) (2011) 809-814. https://doi.org/10.1038/Nnano.2011.186.

[20] M.J. Rosenbluth, W.A. Lam, D.A. Fletcher, Force microscopy of nonadherent cells: a comparison of leukemia cell deformability, Biophys. J. 90(8) (2006) 2994-3003. https://doi.org/10.1529/biophysj.105.067496.

[21] M. Lekka, Discrimination Between Normal and Cancerous Cells Using AFM, Bionanoscience 6(1) (2016) 65-80. https://doi.org/10.1007/s12668-016-0191-3.

[22] J. Rheinlaender, S. Vogel, J. Seifert, M. Schachtele, O. Borst, F. Lang, M. Gawaz, T.E. Schaffer, Imaging the elastic modulus of human platelets during thrombin-induced activation using scanning ion conductance microscopy, Thromb. Haemostasis 113(2) (2015) 305-311. https://doi.org/10.1160/Th14-05-0414.

[23] X. Liang, G. Mao, K.Y. Ng, Mechanical properties and stability measurement of cholesterol-containing liposome on mica by atomic force microscopy, J. Colloid Interface Sci. 278(1) (2004) 53-62. https://doi.org/10.1016/j.jcis.2004.05.042.

[24] F. Tokumasu, A.J. Jin, G.W. Feigenson, J.A. Dvorak, Atomic force microscopy of nanometric liposome adsorption and nanoscopic membrane domain formation, Ultramicroscopy 97(1-4) (2003) 217-27. https://doi.org/10.1016/S0304-3991(03)00046-9.

[25] O. Et-Thakafy, N. Delorme, F. Guyomarc'h, C. Lopez, Mechanical properties of milk sphingomyelin bilayer membranes in the gel phase: Effects of naturally complex heterogeneity, saturation and acyl chain length investigated on liposomes using AFM, Chem. Phys. Lipids 210 (2018) 47-59. https://doi.org/10.1016/j.chemphyslip.2017.11.014.

[26] D.E. Laney, R.A. Garcia, S.M. Parsons, H.G. Hansma, Changes in the elastic properties of cholinergic synaptic vesicles as measured by atomic force microscopy, Biophys. J. 72(2) (1997) 806-813. https://doi.org/10.1016/S0006-3495(97)78714-9.

[27] S. Sharma, H.I. Rasool, V. Palanisamy, C. Mathisen, M. Schmidt, D.T. Wong, J.K. Gimzewski, Structural-Mechanical Characterization of Nanoparticle Exosomes in Human Saliva, Using Correlative AFM, FESEM, and Force Spectroscopy, ACS Nano 4(4) (2010) 1921-1926. https://doi.org/10.1021/nn901824n.

[28] S. Sharma, K. Das, J. Woo, J.K. Gimzewski, Nanofilaments on glioblastoma exosomes revealed by peak force microscopy, J. R. Soc. Interface 11(92) (2014) 20131150. https://doi.org/10.1098/rsif.2013.1150.

[29] M.C. Yadav, M. Bottini, E. Cory, K. Bhattacharya, P. Kuss, S. Narisawa, R.L. Sah, L. Beck, B. Fadeel, C. Farquharson, J.L. Millan, Skeletal Mineralization Deficits and Impaired Biogenesis and Function of Chondrocyte-Derived Matrix Vesicles in Phospho1(-/-) and Phospho1/Pi t1 Double-Knockout Mice, J. Bone Miner. Res. 31(6) (2016) 1275-86. https://doi.org/10.1002/jbmr.2790.

[30] M. Bolean, I.A. Borin, A.M.S. Simao, M. Bottini, L.A. Bagatolli, M.F. Hoylaerts, J.L. Millan, P. Ciancaglini, Topographic analysis by atomic force microscopy of proteoliposomes matrix vesicle mimetics harboring TNAP and AnxA5, Biochim. Biophys. Acta Biomembr. 1859(10) (2017) 1911-1920. https://doi.org/10.1016/j.bbamem.2017.05.010.

[31] M. Bolean, A.M. Simao, T. Kiffer-Moreira, M.F. Hoylaerts, J.L. Millan, R. Itri, P. Ciancaglini, Proteoliposomes with the ability to transport Ca(2+) into the vesicles and hydrolyze phosphosubstrates on their surface, Arch. Biochem. Biophys. 584 (2015) 79-89. https://doi.org/10.1016/j.abb.2015.08.018.

[32] A. Strzelecka-Kiliszek, L. Bozycki, S. Mebarek, R. Buchet, S. Pikula, Characteristics of minerals in vesicles produced by human osteoblasts hFOB 1.19 and osteosarcoma Saos-2 cells stimulated for mineralization, J. Inorg. Biochem. 171 (2017) 100-107. https://doi.org/10.1016/j.jinorgbio.2017.03.006.

[33] D. Vorselen, F.C. MacKintosh, W.H. Roos, G.J.L. Wuite, Competition between Bending and Internal Pressure Governs the Mechanics of Fluid Nanovesicles, ACS Nano 11(3) (2017) 2628-2636. https://doi.org/10.1021/acsnano.6b07302.

[34] J.L. Hutter, J. Bechhoefer, Calibration of atomic-force microscope tips, Review of Scientific Instruments 64(7) (1993) 1868-1873. https://doi.org/10.1063/1.1143970.

[35] H.J. Butt, M. Jaschke, Calculation of thermal noise in atomic force microscopy, Nanotechnology 6(1) (1995) 1-7. https://doi.org/10.1088/0957-4484/6/1/001.

[36] R. Lévy, M. Maaloum, Measuring the spring constant of atomic force microscope cantilevers: thermal fluctuations and other methods, Nanotechnology 13(1) (2002) 33-37. https://doi.org/10.1088/0957-4484/13/1/307.

[37] R. Proksch, T.E. Schäffer, J.P. Cleveland, R.C. Callahan, M.B. Viani, Finite optical spot size and position corrections in thermal spring constant calibration, Nanotechnology 15(9) (2004) 1344-1350. https://doi.org/10.1088/0957-4484/15/9/039.

[38] T.E. Schäffer, Calculation of thermal noise in an atomic force microscope with a finite optical spot size, Nanotechnology 16(6) (2005) 664-670. https://doi.org/10.1088/0957-4484/16/6/007.

[39] D.A. Walters, J.P. Cleveland, N.H. Thomson, P.K. Hansma, M.A. Wendman, G. Gurley, V. Elings, Short cantilevers for atomic force microscopy, Review of Scientific Instruments 67(10) (1996) 3583-3590. https://doi.org/10.1063/1.1147177.

[40] B.J. Briscoe, K.S. Sebastian, M.J. Adams, The Effect of Indenter Geometry on the Elastic Response to Indentation, J. Phys. D Appl. Phys. 27(6) (1994) 1156-1162. https://doi.org/10.1088/0022-3727/27/6/013.

[41] I.N. Sneddon, The relation between load and penetration in the axisymmetric boussinesq problem for a punch of arbitrary profile, Int. J. Eng. Sci. 3(1) (1965) 47-57. https://doi.org/10.1016/0020-7225(65)90019-4.

[42] H. Hertz, Über die Berührung fester elastischer Körper, J. Reine Angew. Math 92(1882) (1882) 156-171. https://doi.org/10.1515/crll.1882.92.156.

[43] W.C. Oliver, G.M. Pharr, An improved technique for determining hardness and elastic modulus using load and displacement sensing indentation experiments, J. Mater. Res. 7(06) (1992) 1564-1583. https://doi.org/10.1557/jmr.1992.1564.

[44] W. Gindl, T. Schöberl, The significance of the elastic modulus of wood cell walls obtained from nanoindentation measurements, Composites Part A: Applied Science and Manufacturing 35(11) (2004) 1345-1349. https://doi.org/10.1016/j.compositesa.2004.04.002.

[45] A. Touhami, B. Nysten, Y.F. Dufrêne, Nanoscale Mapping of the Elasticity of Microbial Cells by Atomic Force Microscopy, Langmuir 19(11) (2003) 4539-4543. https://doi.org/10.1021/la034136x.

[46] M.E. Dokukin, N.V. Guz, I. Sokolov, Quantitative study of the elastic modulus of loosely attached cells in AFM indentation experiments, Biophys. J. 104(10) (2013) 2123-31. https://doi.org/10.1016/j.bpj.2013.04.019.

[47] T. Jadidi, H. Seyyed-Allaei, M.R. Tabar, A. Mashaghi, Poisson's Ratio and Young's Modulus of Lipid Bilayers in Different Phases, Front. Bioeng. Biotechnol. 2 (2014) 8. https://doi.org/10.3389/fbioe.2014.00008.

[48] N. Nijenhuis, X. Zhao, A. Carisey, C. Ballestrem, B. Derby, Combining AFM and acoustic probes to reveal changes in the elastic stiffness tensor of living cells, Biophys. J. 107(7) (2014) 1502-12. https://doi.org/10.1016/j.bpj.2014.07.073.

[49] C. Thouverey, G. Bechkoff, S. Pikula, R. Buchet, Inorganic pyrophosphate as a regulator of hydroxyapatite or calcium pyrophosphate dihydrate mineral deposition by matrix vesicles, Osteoarthr. Cartilage 17(1) (2009) 64-72. https://doi.org/10.1016/j.joca.2008.05.020.

[50] M.F. Hoylaerts, S. Van Kerckhoven, T. Kiffer-Moreira, C. Sheen, S. Narisawa, J.L. Millan, Functional significance of calcium binding to tissue-nonspecific alkaline phosphatase, PLoS One 10(3) (2015) 1911-1920. https://doi.org/10.1371/journal.pone.0119874.

[51] B.R. Genge, G.R. Sauer, L.N.Y. Wu, F.M. Mclean, R.E. Wuthier, Correlation between Loss of Alkaline-Phosphatase Activity and Accumulation of Calcium during Matrix Vesicle-Mediated Mineralization, Journal of Biological Chemistry 263(34) (1988) 18513-18519.

[52] J.M. Cotmore, G. Nichols, Jr., R.E. Wuthier, Phospholipid-calcium phosphate complex: enhanced calcium migration in the presence of phosphate, Science 172(3990) (1971) 1339-41. https://doi.org/10.1126/science.172.3990.1339.

[53] T. Kirsch, H.D. Nah, D.R. Demuth, G. Harrison, E.E. Golub, S.L. Adams, M. Pacifici, Annexin V-mediated calcium flux across membranes is dependent on the lipid composition: Implications for cartilage mineralization, Biochemistry-Us 36(11) (1997) 3359-3367. https://doi.org/10.1021/bi9626867.

[54] M. Bolean, A.M.S. Simao, M.B. Barioni, B.Z. Favarin, H.G. Sebinelli, E.A. Veschi, T.A.B. Janku, M. Bottini, M.F. Hoylaerts, R. Itri, J.L. Millan, P. Ciancaglini, Biophysical aspects of

biomineralization, Biophys. Rev. 9(5) (2017) 747-760. https://doi.org/10.1007/s12551-017-0315-1.

[55] V. Uskokovic, R. Odsinada, S. Djordjevic, S. Habelitz, Dynamic light scattering and zeta potential of colloidal mixtures of amelogenin and hydroxyapatite in calcium and phosphate rich ionic milieus, Arch. Oral Biol. 56(6) (2011) 521-32. https://doi.org/10.1016/j.archoralbio.2010.11.011.

[56] B.B. Weiner, W.W. Tscharnuter, D. Fairhurst, Zeta potential: a new approach, Canadian Mineral Analysts Meeting, Brookhaven Instruments Corporation, Winnipeg, Canada, 1993.

[57] J.D. Clogston, A.K. Patri, Zeta potential measurement, in: S. McNeil (Ed.), Characterization of Nanoparticles Intended for Drug Delivery, Humana Press, New York, 2011, pp. 63-70. https://doi.org/10.1007/978-1-60327-198-1_6.

[58] A.M.S. Simao, M. Bolean, B.Z. Favarin, E.A. Veschi, C.B. Tovani, A.P. Ramos, M. Bottini, R. Buchet, J.L. Millan, P. Ciancaglini, Lipid microenvironment affects the ability of proteoliposomes harboring TNAP to induce mineralization without nucleators, J. Bone Miner. Metab. (2018). https://doi.org/10.1007/s00774-018-0962-8.